# 1

# Introduction

## 1.1 Nanomaterials

Natural beings, be it, humans, animals, plants, insects, etc. are the most efficient and greatest invention of all time. It is the synergy of all the nanoscopic matter within these beings that makes them to the level of perfection which researchers around the world are trying to mimic for decades. Nanomaterials are one of the key materials to mimic natural systems as the basic unit of all the natural systems is in the nano-range. The word "nano" is derived from the Greek word meaning "dwarf" and resembles objects in the $10^{-9}$ m in scale [Kolahalam et al., 2019]. Nanomaterials have gained attention in the latest century due to their enhanced and easily tunable physical, chemical, electrical, mechanical, optical, etc. properties in comparison to their bulk counterparts. These exceptional properties of nanomaterials are ascribed to the tremendous enhancement in surface to volume ratio and quantum confinement due to the discretization of energy levels with the decrease in particle size.

## 1.2 Nanomaterials for Energy Applications

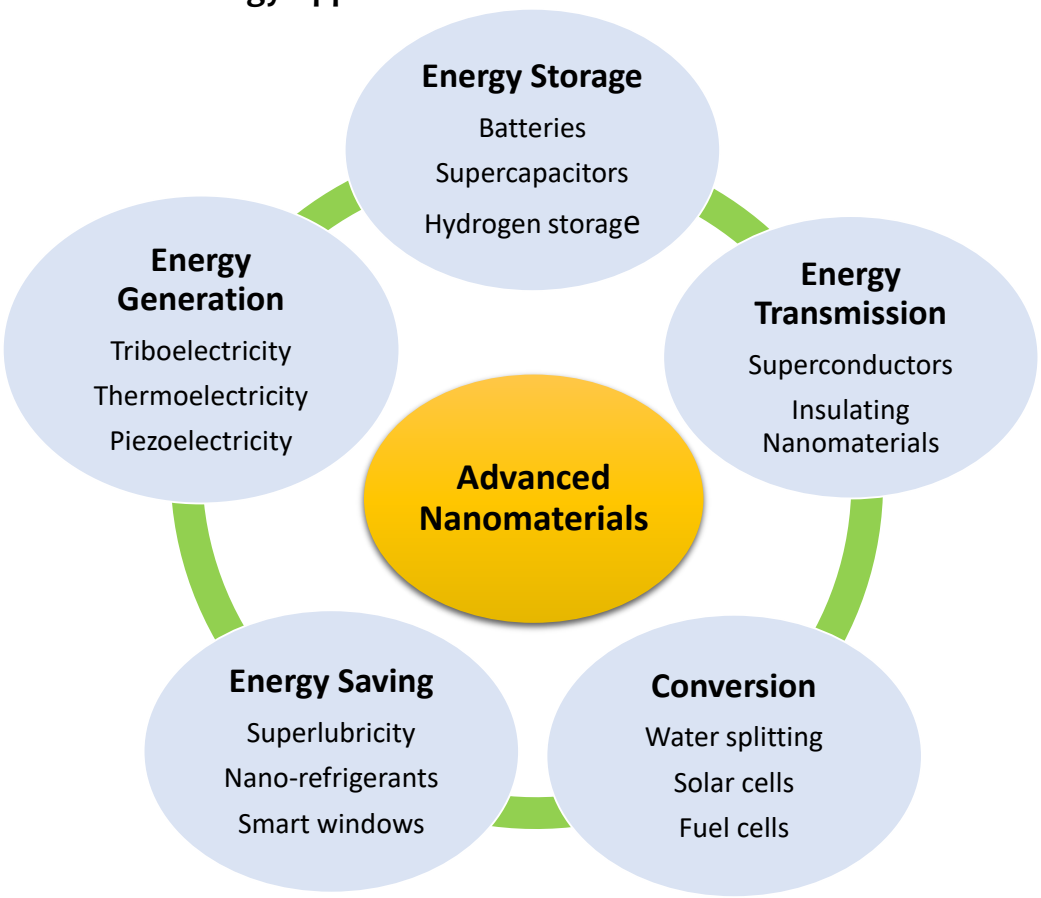


**Figure 1.1:** Application of nanomaterials in various energy applications.

Serious challenges are being faced all around the globe for optimum utilization of energy due to the ever-increasing global population, which is expected to reach 9 billion by 2050 [van Ruijven

et al., 2019]. Hence, there is a need for alternative sources and storage of energy for efficient and uninterrupted energy production, transmission, and storage. Renewable sources of energy, including solar, wind, tidal, geothermal, and biomass, are being explored all around the world for alternate sources. However, the efficiency of the conversion is still far from par. Energy storage capability post-conversion to electrical energy in batteries and supercapacitors is still a challenge. Further, the losses during the transmission of energy are enormous. The efficiency of energy materials is directly influenced by the type of material and its chemical, electrical, mechanical, thermal, optical, and catalytic activity. Hence, there is an urgent requirement for advanced materials for efficient utilization in various energy applications. Nanomaterials, due to their exceptional electrical and thermal conductivity, large surface area, and chemical stability are highly competitive in energy applications (Figure 1.1). Nanomaterials of different chemical compositions are making a major contribution to photovoltaics, thermoelectric, triboelectric, energy storage, electrocatalytic, piezoelectric materials, thus facilitating the energy industry immensely [Wang et al., 2020]. The advancement in the field of nanotechnology has resulted in a fine level of tunability in the material properties for advanced energy applications. Overall, with the advent of nanotechnology, a significant enhancement is observed in the energy sector in terms of production, conversion, storage and transmission of energy. The recent advances in energy devices have the potential to flourish further by tailoring the properties in the nanoscale for advanced energy materials.

## 1.3 Nanomaterials for Gas Sensors

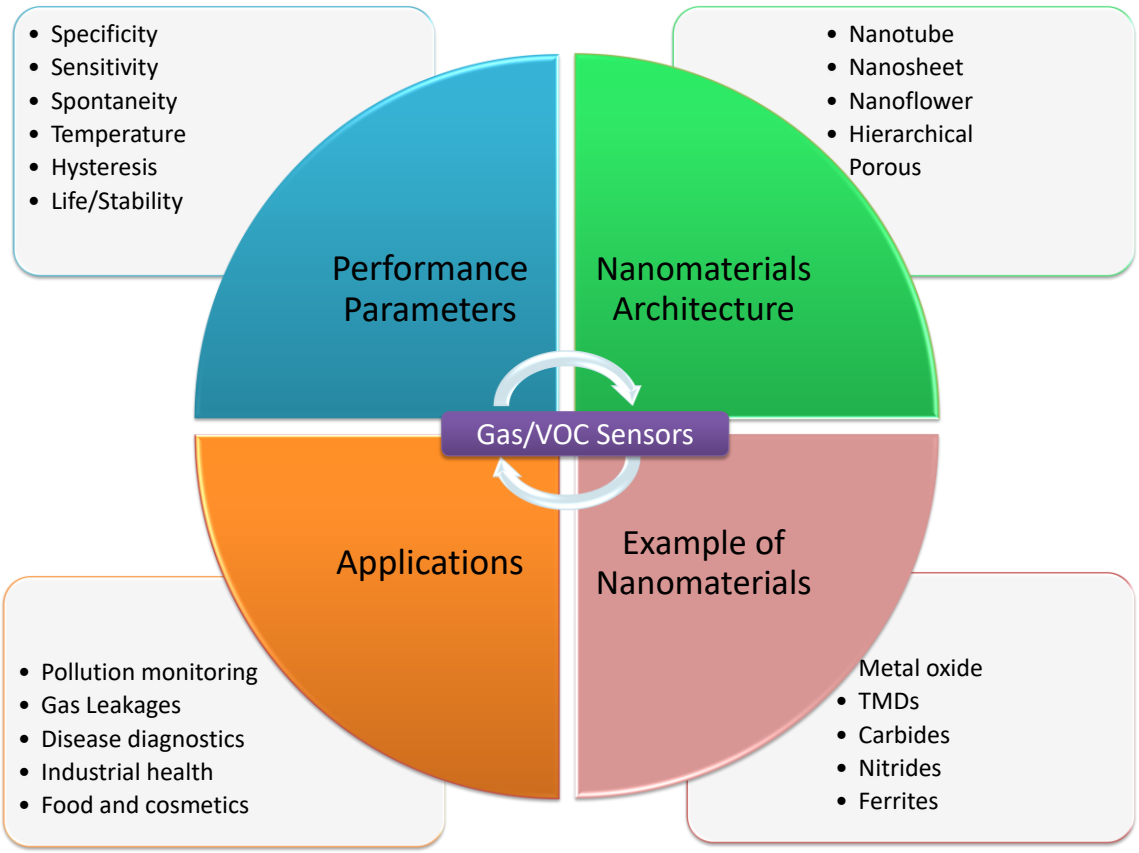


**Figure 1.2:** Important parameters of nanomaterials for gas/VOC sensors.

Fresh air is an indispensable requirement for the well being of humans. However, with the advancement of human generation and the rising population leading to socioeconomic growth around the globe, the air quality is drastically deteriorating at an alarming rate. It is thus very important to continuously monitor indoor and outdoor air quality for a healthy lifestyle Conventionally, the air quality is analyzed using gas chromatography-mass spectroscopy (GC-MS) and photoionization detectors, which are bulky, and require specialized manpower for

instrument handling [Spinelle et al., 2017]. Scientists around the world are working on discovering advanced materials and devices for efficient, reliable, and handy detection of various gases/volatile organic compounds (VOCs). Apart from the application of gas/VOCs sensors for environmental monitoring, highly sensitive VOC sensors with a low limit of detection are also being explored in the healthcare sector for non-invasive detection of various diseases by sensing biomarkers from exhaled human breath [Yan et al., 2019]. Different materials have been explored as gas sensors since the 1950s, and the never-ending quest for a better sensing material in terms of sensitivity, selectivity, spontaneity has lead to significant advancements (Figure 1.2). Nanoforms of different materials have been one of the most efficient gas/VOC sensors due to the wide range of exceptional properties that are induced due to high surface area, defects, enhanced charge transport, specific catalytic sites for analyte adsorption, etc. Active materials have been grown in the form of different morphologies with nanotubes, nanorods, nanofibers, nanowires, nanosheets, nanoflowers, hierarchical, porous, etc. structures and has shown tremendous improvements in the gas sensing performance [Malik et al., 2020]. Nano forms of metal oxides, nitrides sulfides, selenides, ferrites have been extensively studied with some new materials like phosphorene, carbon organic frameworks, photonic crystals, ferrocene, quantum dots and black phosphorous. Undisputably nanoforms of metal oxides based gas sensors have ruled the sensing industry since the inception. There have been significant advancements in gas sensing technology, still, there are numerous challenges like working temperature, selectivity, and long term reliability that need to be addressed.

## 1.4 Modification of Nanomaterials by Doping

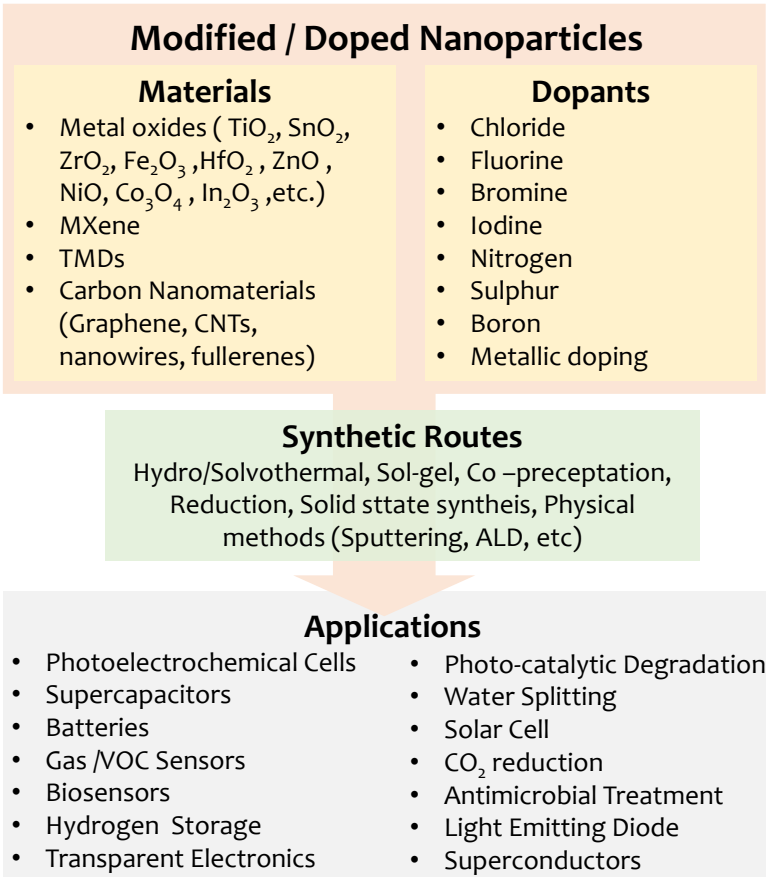


**Figure 1.3:** Overview of doped nanomaterials for different applications.

As highlighted in section 1.2 and 1.3, nanomaterials have played a significant role in revolutionalizing energy and sensing technology. However, with the continuous increment in human demands, there is a need for new nanomaterials that can withstand the rising requirements. Doping of nanomaterials is one of the viable and easy approach of tuning the material properties as per requirements. Nanomaterials can be doped using boh metallic and

non-metallic sources for tuning the material properties (Figure 1.3). Metallic doping includes transition metals, post-transition metals, rare earth metals, alkali metals, and noble metals, including Pt, Ag, and Au. Inorganic dopants mostly include the halides (chlorine, fluorine, bromine, iodine), nitrogen, sulfur, phosphorous, carbon, selenium, and tellurium. In metal oxides, the inorganic dopants usually substitute the oxygen in the metal oxide lattice or the parent metal or occupy an interstitial site inducing strain. In the carbon matrix, doping with metalling and non-metallic dopants can change the bonding characteristics and thus inducing electrical, optical, mechanical, and electrochemical alterations. Doping of materials can induce significant changes in the crystal structure of the parent material. The electronic structure is altered due to the introduction of new band states in the parent nanostructure usually leading to narrowing of band gap. Dopants also induce enhanced catalytic properties by changing the surface properties of the metals oxide nanoparticles. Oxygen vacancies in metal oxides play a significant role in deciding the efficiency of the metal oxide-based devices are easily tuned by doping. Trap states in the materials can be optimized in accordance with the requirement. Doping of nanomaterials can also provide structural and morphological stability, thus enhancing the performance of nanodevices for longer times. Further, properties arising due to doping can be easily tuned due to the flexibility of doping percentages leading to widespread applicability of doped materials. For these reasons, doped materials have been explored in almost every application, including energy, sensors, biological applications, thermal plants, catalysis, etc. (Figure 1.3).

## 1.5 Fluorine as a Dopant

Fluorine, a halide group element with an atomic mass of 19, is one of the interesting elements in the periodic table. Fluorine chemistry started long ago with the discovery of fluorine in 1886 by French chemist Henri Moissan. The greatest inventions in history have the backbone of fluorine as an important moiety in the chemical composition of the technology developed. One of the well-known examples is of Teflon, which is being used in one or the other way in almost every sphere of living, including household, laboratory, technology, etc. Fluorine is known to be the most electronegative element in the periodic table. Oxygen is the second most electronegative element and, when replaced by fluorine in the material lattice and can give rise to exceptional properties. Fluorine can be present in the material in two ways i.e., lattice doped or surface fluorine, which is highly dependent on the synthesis procedure adopted for fluorination. Fluorine doping can be in the following forms [McCabe et al., 2007]:

*Substitutional Doping:*
(1) Reductive anion exchange: one $O^{2-}$ anion is substituted by one $F^{-}$ anion, resulting in a reduction of the metal oxide lattice
(2) Anion exchange: one $O^{2-}$ anion is substituted by two $F^{-}$ anions, causing neither oxidation or reduction of the metal lattice
*Interstitial doping:*
(3) Oxidative anion insertion: insertion of $F^{-}$ into interstitial sites, requiring oxidation of metal oxide lattice
(4) Structural rearrangement following (1)–(3), the site preferences of oxygen and fluorine may drive a rearrangement of the metal oxide structure.

In the case of fluorination of carbon materials, fluorine has even high binding energy with carbon than that of hydrogen to carbon, making the carbon-fluorine bond even more stable than the carbon-hydrogen bond [Kemnitz et al., 1998]. The chemistry of fluorine is interesting and the scientists believe that there is much more that is yet to be explored for better living of the world. Incorporation of even a small amount of fluorine into a matrix can impart unexpected properties to a material. Fluorination of inorganic nanomaterials using solution-processable sources is a challenge. The tendency of M-F bond formation is lower than that of M-O bonds due to the extreme hardness of $F^{-}$ in comparison to $HO^{-}$, thus, conjugating less with most of the

soft/intermediate metal ions. For this reason, direct fluorination using reactive, toxic gaseous fluorine sources ($F_2$, $XeF_2$, $SF_6$ gas) has been dominantly reported in the literature [Brink et al., 2000; Zhou et al., 2015a]. Fluorination using conventional (nucleophilic) solution-processable sources leads to oriented growth in a specific crystal direction rather than fluorine incorporation [Lv et al., 2010, 2011; Yang et al., 2008]. In the following sections, fluorination of inorganic compounds, including metal oxides and carbon, will be discussed along with the synthesis routes, advantages and applications of fluorination.

## 1.6 Advantages and Application of Fluorination

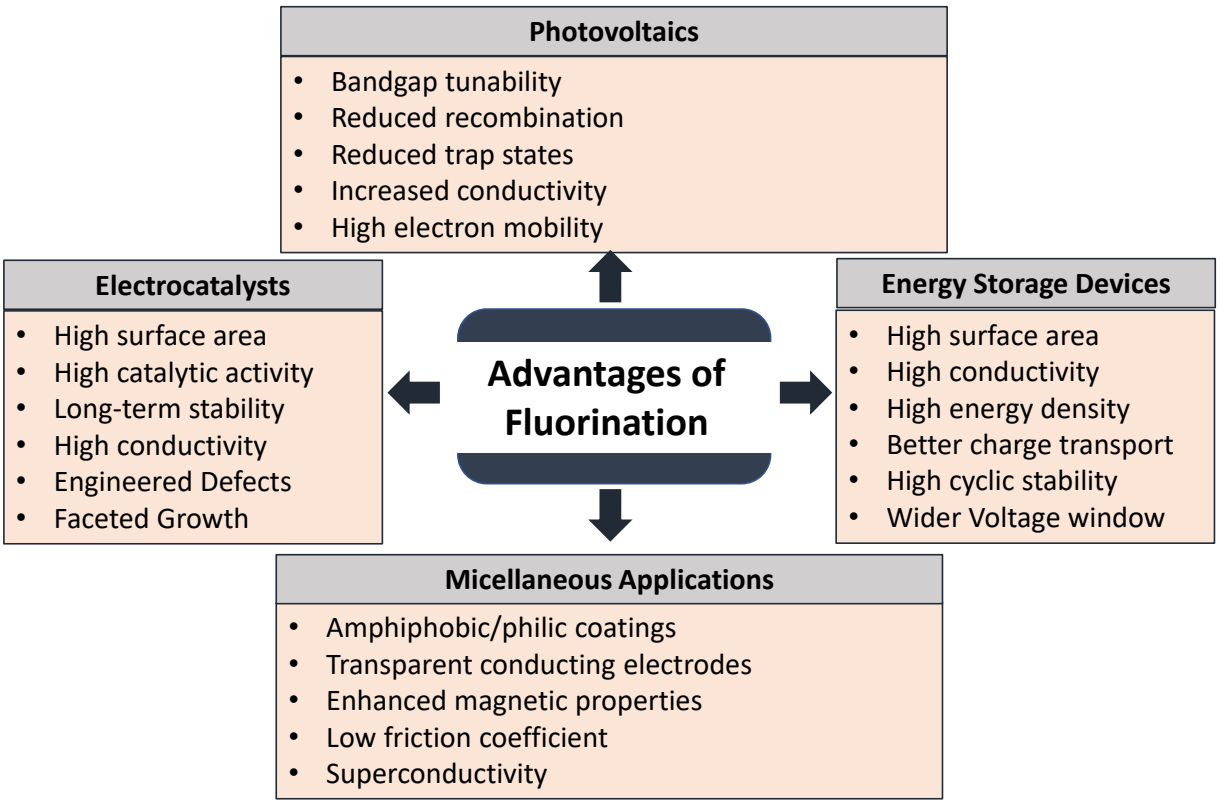


**Figure 1.4:** Advantages of fluorination for different applications.

### 1.6.1 Fluorinated Metal Oxides

Fluorinated inorganic materials find a wide variety of applications due to their exceptional and tunable properties. $F^-$ with a similar ionic radius (133 pm) as that of $O^{2-}$ (140 pm), has been suggested to be one of the most adequate anion dopants for metal oxides because of its lower lattice distortion compared with other alternatives. Due to ever-increasing energy demand, there has been increasing efforts on energy production and storage. Fluorinated metal oxides are one of the emerging material for energy applications, including photovoltaics, batteries, supercapacitors, and water splitting (Figure 1.4). Extrinsic fluorine anion doping of semiconducting metal oxides such as $SnO_2$, $TiO_2$, $Co_3O_4$, and $Fe_2O_3$ have turned out as an important route for surface passivation of metal oxides that inhibits $e^-/h^+$ recombination and improves charge carriers mobility. Additionally, fluorine doping is expected to achieve tunable optical absorption and a modified band position for enhancement in the photoelectrochemical activity. For example, Gasparotto *et al.* [Gasparotto et al., 2011] synthesized fluorine-doped $Co_3O_4$ by plasma-enhanced chemical vapor deposition method using fluorinated β-diketonate cobalt derivative as a single fluorine and cobalt precursor and observed a significant improvement in hydrogen production. Similarly, Choi *et al.* carried out fluorination of $TiO_2$ using sodium fluoride for enhanced photocatalytic action [Park et al., 2004]. The enhancement in catalytic activity is understandable due to the increase in Lewis acidity of Fe-centers by substitution of surface oxygen atoms with fluorine. Wang *et al.* observed rapid photocatalytic

degradation of Rhodamine dye using fluorinated $SnO_2$ [Wang et al., 2015b]. Karthikeyan *et al.* synthesized F, N-doped $Fe_2O_3$ using ammonium fluoride, and urea and used it for supercapacitor application [Karthikeyan et al., 2014]. Several fluorine-doped metal oxides have been synthesized in order to enhance the electrochemical performance of batteries [McCabe et al., 2007]. It is anticipated that the replacement of $O^{2-}$ by anions, with $F^-$ can effectively reduce the materials' electric resistivity and inhibit lattice changes during cycling, which results in significantly improved cycling life and rate capability [Liu et al., 2017a].

### 1.6.2 Fluorocarbons

These are extensively used in energy conversion and storage devices like batteries, supercapacitors, fuel cells and photoelectrochemical solar cells. In 1972, fluorocarbons were first used as a cathode in lithium primary batteries, and $Li/CF_x$ batteries were first commercialized in Japan in 1975. After that, fluorocarbons tend to replace the conventional carbon materials as electrodes because of their unique properties, such as high energy density, wide operating voltage, long shelf life, stable operation ability, and better capacitance value (Figure 1.4). Among them, fluorinated graphene is regarded as the most promising $CF_x$ to achieve the theoretical capacity because of large specific surface area and favorable diffusion kinetics of lithium ions [Bi et al., 2018]. It behaves as a typical semiconductor with a tunable bandgap and finds application in solar cells [Jeon et al., 2011]. Along with that, fluorinated graphene quantum dots exhibits unique electronic and luminescent properties because of quantum confinement and edge effects. Recently, fluorocarbons doped with another heteroatom such as nitrogen, boron, phosphorus, bromine are also gaining momentum as an electrode material because of better electrochemical performance [Huang et al., 2015]. They are also being used for application in supercapacitors, electrochemistry and amphiphobic coatings [Na et al., 2017; Zhou et al., 2016]. In the literature, it is known that the heterogeneous electron transfer accelerates by increasing the F/C ratio, which enhances its role as an electrocatalyst [Boopathi et al., 2014]. The fluorinated and co-doped carbons are also extensively explored as electrocatalyst for ORR in fuel cells [Lv et al., 2017]. The fluorocarbons are of many interest in many bio applications such as fluorinated graphene as the scaffold for the growth of mesenchymal stem cells.

## 1.7 Literature Survey

### 1.7.1 Fluorination of Carbon Materials

Carbon nanomaterials are an important class of nanomaterials which shows different properties depending on their allotropic form. The properties of carbon nanomaterials can be tuned by functionalization or doping that can significantly alter their hybridization, stacking, packing and crystallite size (Figure 1.5). Fluorination of graphene, graphene oxide, carbon nanotubes and activated carbon is a topic of immense interest due to the exciting properties that emerge from these modified materials due to the changes in the nature of $sp^2$ hybridization [Adamska et al., 2017; Feng et al., 2016; Guérin et al., 2004; Lee, 2007]. The introduction of fluorine into carbon framework amends the physical and chemical properties making them suitable for a wide variety of applications such as electrode for energy storage devices, magnetic resonance imaging, hydrogen storage, electrocatalysis for water splitting and fuel cells [Boopathi et al., 2014; Ho et al., 2015; Jeon et al., 2015; Lv et al., 2017; Wang et al., 2014; Zhou et al., 2016]. Due to the high electronegativity of fluorine atoms, the surface polarity increases ion transportation, facilitate electrical conductivity, improve charge mobility, decrease charge transfer resistance and enhances surface wettability [Feng et al., 2016; Liu et al., 2018a; Na et al., 2017; Wang et al., 2014; Zhou et al., 2015b].

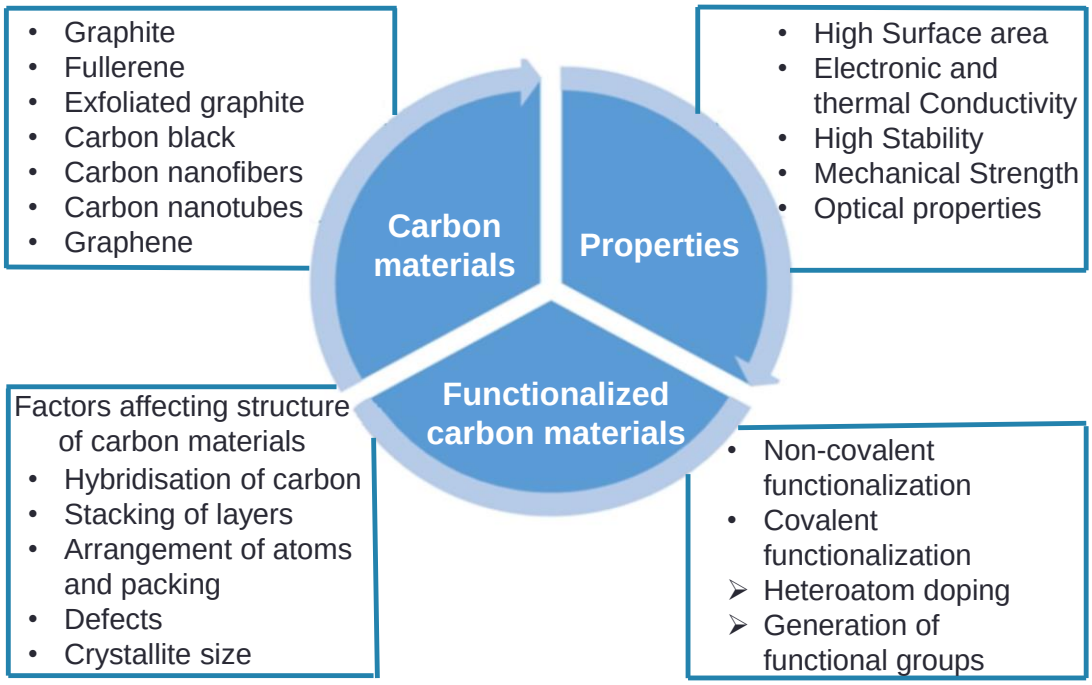


**Figure 1.5:** Properties and functionalization of carbon materials.

The fluorination process can alter the charge distribution on carbon which has a direct impact on its electrochemical performance [Bruna et al., 2011; Cheng et al., 2009; Zbořil et al., 2010]. Fluorocarbons exhibit various kinds of C-F bonds from ionic to semi-ionic to covalent bonds because of the high electronegative difference (1.5) between C and F atoms and also have different F/C ratios which can be tuned by synthetic methods and fluorination conditions (Figure 1.6).

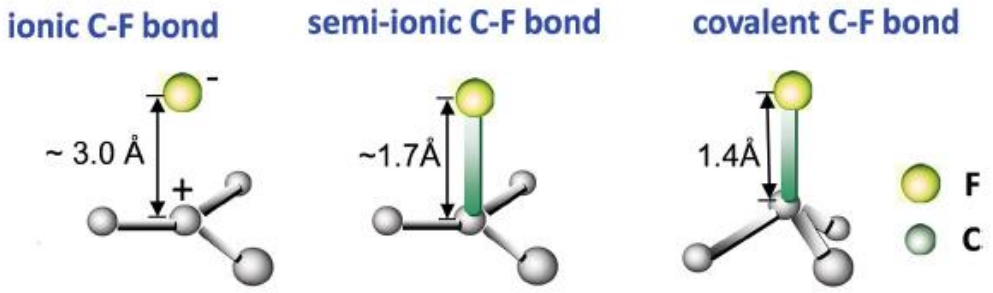


**Figure 1.6:** Different C-F bonds and their bond lengths. Figure adapted from reference [Feng et al., 2016].

By optimizing the C-F bonding character and F/C ratios, one can control the properties and design the application of fluorocarbons [Chia et al., 2014; Nair et al., 2010; Zbořil et al., 2010]. The semi-ionic bonding increases the electrical conductivity resulting in an improvement in electrochemical double layer capacitance [An et al., 2016; Kim et al., 2014; Zhou et al., 2016]. Fluorinated carbon materials are evolving as one of the significant outcome of the functionalized graphene family due to its property of visible range bandgap, increased charge carrier mobility, superhydrophobicity and ultra- high specific surface area. Fluorination of various types of carbon materials such as activated carbon, carbon nanotubes (CNTs), graphene, carbon microspheres, carbon nanofibers, carbon aerogels gives rise to surface doped fluorocarbon which alters its physicochemical properties such solubility, stability, optical, magnetic, mechanical, thermal conductivity, electric and electronic properties [Feng et al., 2016].
Various methods are known for the synthesis of fluorinated carbon materials such as direct gas, photochemical, plasma, solvothermal, hydrothermal, electrochemical fluorination etc. With these methods, one can optimize the physicochemical properties of carbon materials for a particular application by changing the reaction conditions like pressure, temperature, treatment time or the amount of precursor (Figure 1.7).

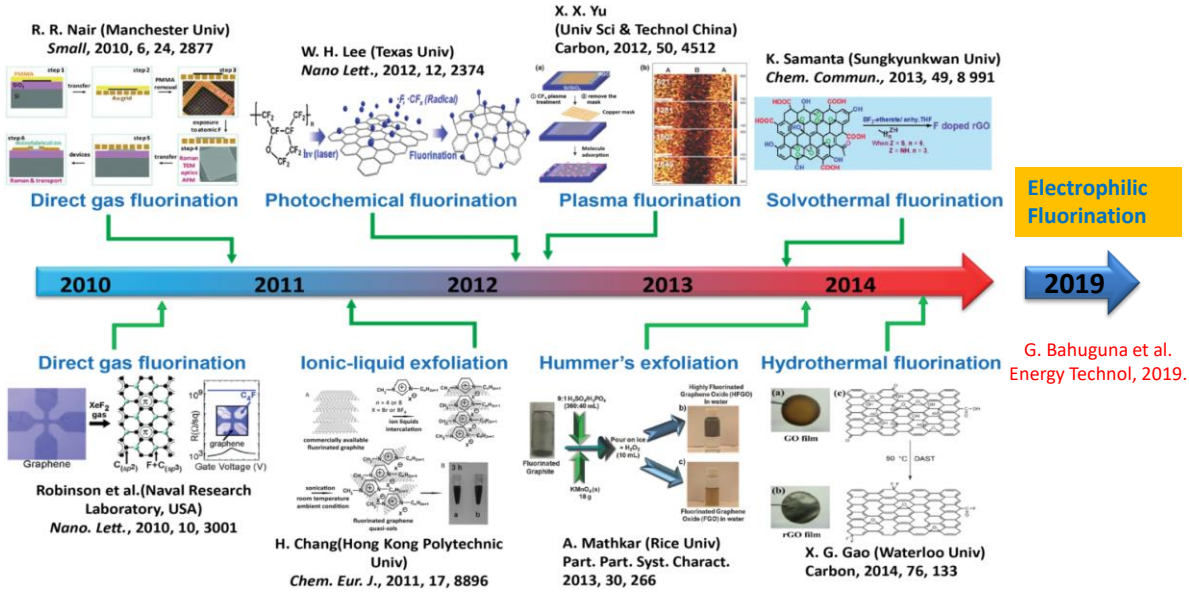


**Figure 1.7:** Synthetic methods and precursors used for fluorination. Figure adapted from reference [Feng et al., 2016].

Direct gas fluorination is the most used and effective method to modify and control the physiochemical properties of carbon material. In literature, different carbon nanomaterial have been fluorinated with $F_2$ gas at elevated temperatures and the amount of fluorine gas controls the F/C ratio of fluorinated carbon. Nair et al. and Jeon *et al.* [Jeon et al., 2011; Nair et al., 2010] explored $F_2$ to fluorinate graphene film at 70 °C and 350 °C for 5 days in inert atmosphere respectively. The large scale production through direct gas fluorination is either restricted by the expensive $XeF_2$ or the poor controllability of C-F bonding characters and F/C ratio by $F_2$ due to its high reactivity. Plasma fluorination compared to direct gas fluorination is an easy to control, mild and clean method for preparation of fluorocarbon. A variety of plasma sources such as $SF_6$, $CF_4$ and $F_2$ are used for generation of fluorine radicals which adsorb onto carbon surface and form different C-F bonds. Another versatile method for preparation of fluorinated carbon is hydrothermal or solvothermal. Fluorination can be controlled by using different fluorinating precursors such as HF, $BF_3$-etherate, and $HPF_6$ etc. Wang *et al.* [Wang et al., 2012] prepared fluorinated dispersed GO using HF through hydrothermal process at different temperatures ranging up to 180 °C. Feng *et al* [Feng et al., 2016] reported photochemical synthesis of selective single-side graphene fluorination using solid fluoropolymer, CYTOP™ and laser irradiation. A brief literature survey of fluorination of carbon material is shown in Table 1.1.

**Table 1.1:** Brief literature survey on various methods adopted for the fluorination of carbon materials.

| S. No. | Carbon Material | Method of doping | Fluorine Precursor | Amount of Fluorine (XPS) | Reference |
|---|---|---|---|---|---|
| 1. | Nitrogen/fluorine codoped mesoporous carbon nanofibers | Hydrothermal and vacuum plasma treatment | PAN/PVP with Octafluoro Cyclobutane gas | 10.9 at% F | [Na et al., 2017] |
| 2. | Multi-walled carbon nanotubes | Thermal fluorination | $F_2$ gas | 7.6 at % F | [Jung et al., 2015] |
| 3. | Bromine- intercalated graphite | Thermal exfoliation | $BrF_3$ in $Br_2$ | 1.4 at % F | [Bulusheva et al., 2014] |
| 4. | Nanoporous Carbon | Gaseous phase reaction | Hydrofluoric acid | 17.5 at % F | [Zhou et al., 2016] |
| 5. | Raw Activated carbon | Gaseous | $F_2$ gas | 0.77 at % F | [Lee, 2007] |

| | | | | | |
|---|---|---|---|---|---|
| | | phase reaction | | | |
| 6. | Raw Activated carbon | Liquid- Phase reaction | 1.0 M Hydrofluoric acid | 0.7 at % F | [Lee, 2007] |
| 7. | Raw Activated Carbon | Liquid-Phase Reaction | 0.1 M Hydrofluoric acid | 0.4 at % F | [Lee, 2007] |
| 8. | Activated carbon fibers | Gaseous phase reaction | $F_2$ gas | 7.0 - 21.7 at % F | [Lee, 2007] |
| 9. | Multi-walled carbon nanotubes (MWCNTs) | Gaseous phase reaction | $F_2$ gas | 13 at % F | [Lee, 2007] |
| 10. | Fluorinated Graphene/ CoAl-layered Double hydroxide Composites | Exfoliation | Hydrofluoric acid | 2.07 at % F | [Peng et al., 2017] |
| 11. | Graphene Hydrogels | Hydrothermal process | Hydrofluoric acid | 4.52 at % F | [An et al., 2016] |
| 12. | Carbon microspheres | Solvothermal reaction | Methyl cyanide, Ammonium Fluoroborate | 3.4 wt% F | [Zhou et al., 2015b] |
| 13. | Phenol-based activated carbon | Gaseous phase reaction | $F_2$ gas | 1.13 at % F | [Jung et al., 2011] |
| 14. | Activated carbon | Gaseous phase reaction | Hydrofluoric acid | 0.7 at% F | [Kim et al., 2014] |
| 15. | Graphene Oxide | Direct gas fluorination | $F_2$ gas | 48.1 at % F | [Wang et al., 2013b] |
| 16. | Graphene | Plasma fluorination | $CF_4$ plasma | 8.9 at % F | [Ho et al., 2015] |
| 17. | Graphene | Chemical vapour deposition | $CF_4$ plasma | 28 at % F | [Wang et al., 2014] |
| 18. | Graphene oxide films | Hydrothermal fluorination | diethylaminosulfurtrifluoride | 3.0-4.0 at% F | [Gao et al., 2014] |
| 19. | Graphene oxide | Thermal treatment | Polyaniline composite $NH_4F$ | 0.13 at% F | [Jiang et al., 2015] |
| 20. | Graphene paper | Solvothermal reaction | Acetonitrile Hydrofluoric acid | 1.65 at% F | [An et al., 2017a] |
| 21. | Graphene oxide | Hydrothermal process | Trimethylamine tri(hydrofluoride) | 10.9 at% F | [Huang et al., 2015] |
| 22. | Reduced graphene oxide | Thermal annealing process | Ammonium fluoride | 0.74 at% F | [Qiao et al., 2016] |

## 1.7.2 Electrolytes in Supercapacitors

There are continuous attempts in the litertaure for understanding and modifying the properties of electrolytes in supercapacitor. For example, *Koh et al.* studied the effect of cationic size in quaternary ammonium salts as electrolytes [Koh et al., 2014]. *Park et al.* used binary salt electrolytes to overcome the electrolyte solubility issues [Park et al., 2017b]. Some of the other examples includes binary mixture of ionic liquid and γ-butyrolactone,[Dagousset et al., 2017] imidazolium-based liquid crystalline electrolyte derived from cashew nut shell liquid [Sasi et al., 2016], graphene quantum dots as liquid and solid state electrolytes, [Zhang et al., 2016b] lithium salt containing organic electrolytes [Zhang et al., 2016c], etc. Moreover, recently there are a lot of studies regarding the redox active electrolytes that include the use of functionalized ionic liquids, [Bodin et al., 2018] redox metal oxide incorporated electrolytes [Hwang et al., 2017], thiocyanates [Gorska et al., 2017], halogenated electrolytes [Gastol et al., 2016], and supramolecular organic fibres [Umesha Mogera, Murali Gedda, 2017].

(a)

| Entry | Product | Yield [%] [a] | Conductivity (mS cm$^{-1}$) [b] | Viscosity (cP) [c] | Entry | Product | Yield [%] [a] | Conductivity (mS cm$^{-1}$) [b] | Viscosity (cP) [c] |
|---|---|---|---|---|---|---|---|---|---|
| 1 | 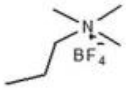 | 78 | 46.9 | 0.57 | 4 | 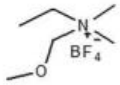 | 68 | 50.8 | 0.56 |
| 2 | 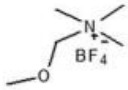 | 50 | 45.9 | 0.57 | 5 | 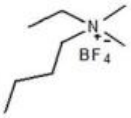 | 63 | 45.3 | 0.61 |
| 3 | 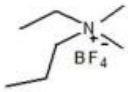 | 50 | 49.8 | 0.56 | 6 | 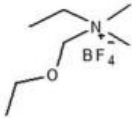 | 53 | 46.3 | 0.60 |

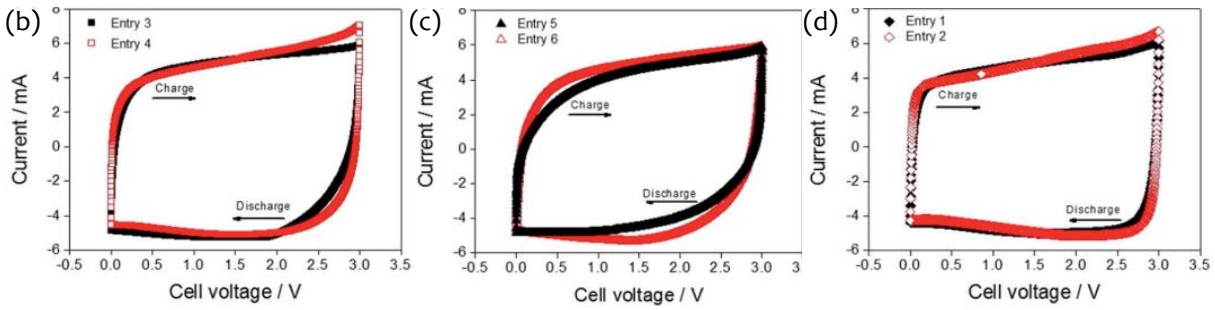


**Figure 1.8:** Physiochemical properties of the quaternary ammonium salts. (b-d) comparative CV plots of heteroatom substituted and un-substituted quaternary ammonium salts shown in (a). Figure adapted from reference [Han et al., 2016].

Addition of heteroatom or redox active molecules to an electrolyte considerably changes the physiochemical properties of an electrolyte [Zhang, 2006]. Han *et al.* and Rennie *et al.*[Rennie et al., 2013] synthesized ether group substituted electrolytes with high performance electrochemical properties. Small electronegative ion containing electrolyte has been reported to show improved electrochemical performance. Han *et al.*[Han et al., 2016] synthesized different quaternary ammonium salts and their ether group substituted counterparts as shown in Figure 1.8a.

The electrolytes were analysed with carbon electrodes in the voltage range between 0-3 V. The CV curves of the substituted counterparts exhibit improved performance in all the three cases (Figure 1.8b-d). By substituting the conventional electrolytes with smaller cations, the capacitance of EDLCs can be remarkably improved as smaller ions can store more energy in microporous carbon material.

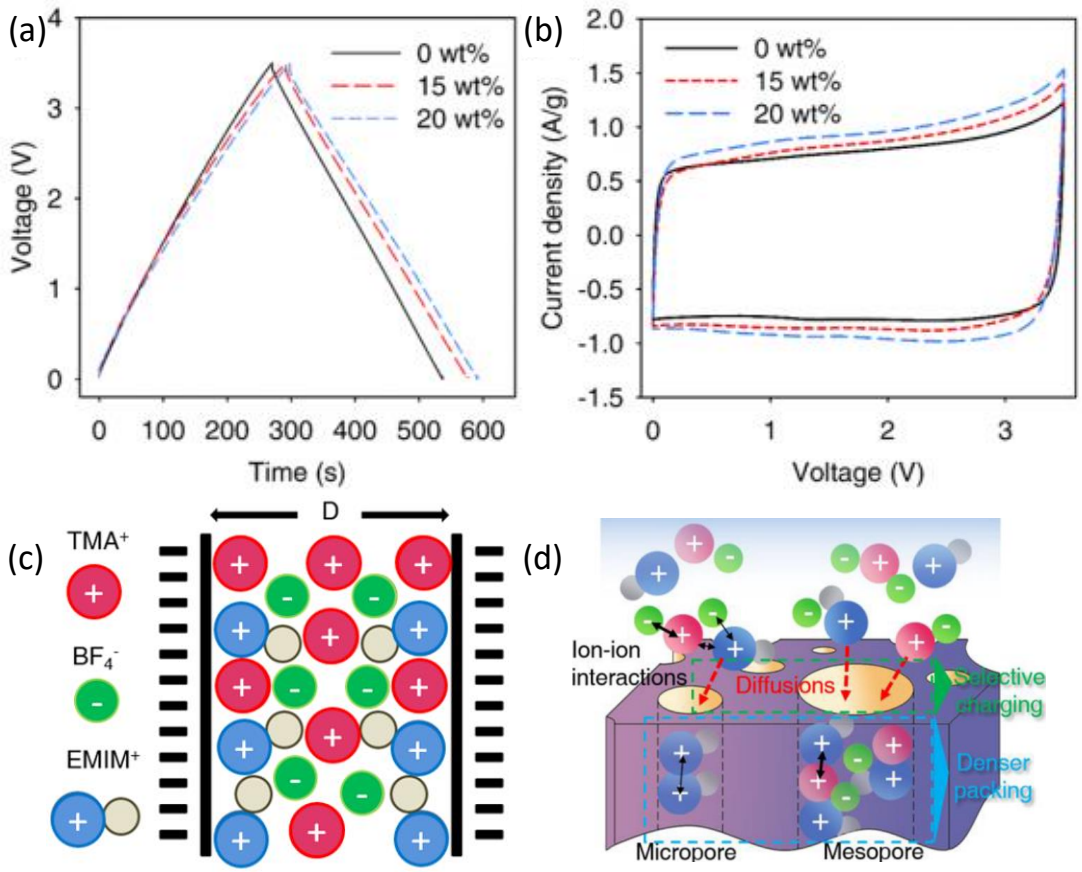


**Figure 1.9:** (a) Galvanostatic charge discharge at 1 A/g and (b) Cyclic voltammogram at 10 mV/s of the mesopore rich carbon. Schematic representation of (c) the mixture electrolyte used in the study and (d) the ionic interaction induced selective charging behavior of ionic mixture electrolyte. Figure adapted from reference [Wang et al., 2017d].

In a very interesting study, the role of mixture electrolytes for efficient supercapacitors was studied by Wang *et al*. [Wang et al., 2017d]. The GCD and CV studies shows an enhancement in GCD and CV characteristics upon increasing the $TMABF_4$ concentration in the $EMIMBF_4$ electrolyte (Figure 1.9a,b). It was reported that different cations in the mixture electrolytes can optimally access both meso and micro pores of the carbon based electrode material. The enhancement in the supercapacitive performance is mainly ascribed to the decrease in ion-ion interaction which can induce fast diffusion, better exploration of micropores and denser packing of the electrolyte ions in the mesopores (Figure 1.9c,d).

### 1.7.3 Humdity Sensors for Healthcare Applications

In general, any material may respond to humidity, but mere interaction with water molecules may not qualify it as a sensor unless it exhibits high sensitivity, specificity, stability, and spontaneity toward the varying amount of moisture content. Hence, there is a need for highly sensitive, specific and stable humidity sensor that can be exploited in healthcare applications. Most of the humidity sensors reported in the literature employ metal oxides [Kuang et al., 2007; Pawar et al., 2015; Zhang et al., 2005], 2D layered transition metals [Smith et al., 2015], carbon nanomaterials [Kafy et al., 2016], polymeric materials [Choi et al., 2015; Park et al., 2017a; Shim et al., 2000; Soomro et al., 2019], polyelectrolytes [Dai et al., 2019b], and supramolecules [Mogera et al., 2014], with the high surface area for reversible adsorption and desorption resulting in high sensitivity.

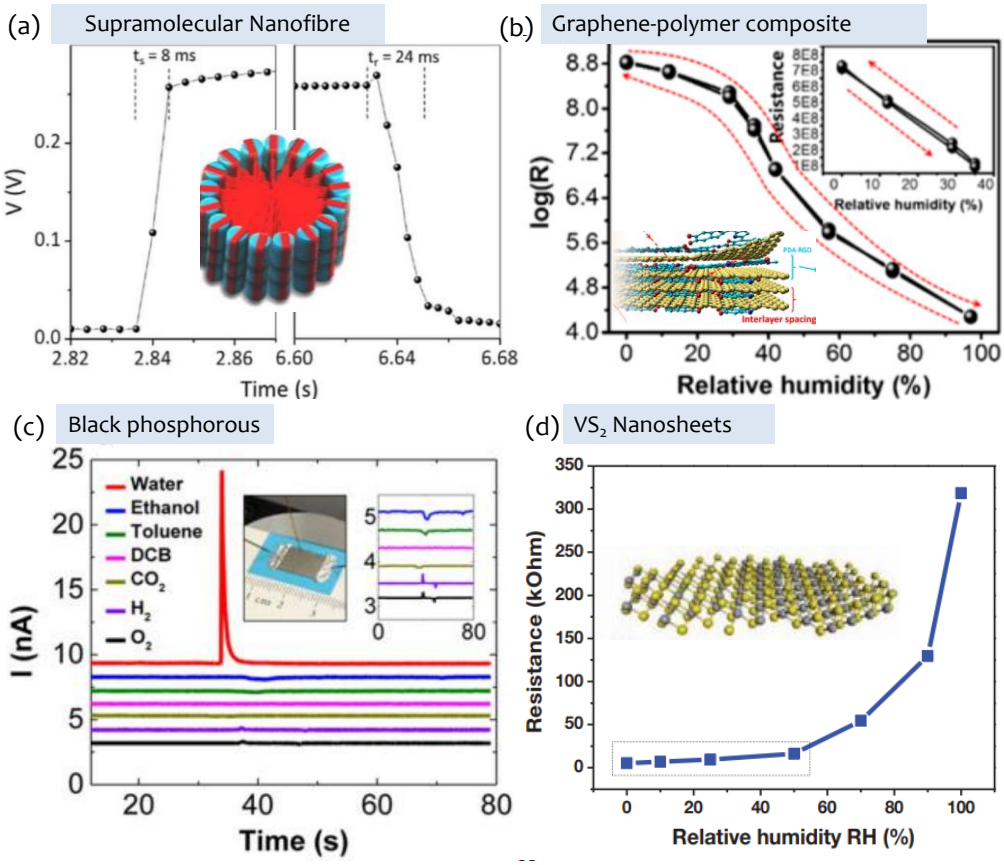


**Figure 1.10:** Humidity sensing characteristics of (a) Supramolecular nanofibre, (b) graphene polymer composite, (c) black phosphorous and (d) $VS_2$ nanosheets based humidity sensors. Figures in a-d are adapted from [Mogera et al., 2014], [He et al., 2018a], [Yasaei et al., 2015b] and {Feng et al., 2012a] respectively.

For example, Mogera *et al.* reported a highly sensitive and ultrafast humidity sensor based on supramolecular charge-transfer nanofibers [Mogera et al., 2014] (Figure 1.10a). He *et al.* reported a graphene-polymer based humidity sensor with four order sensitivity [He et al., 2018a] (Figure 1.10b). Yasaei *et al.* reported a highly selective humidity sensor with minimum response towards other anlytes present in the environment [Yasaei et al., 2015b] (Figure 1.10c). Feng *et al.* reported $VS_2$ based humidity sensor with three order increase in sensitivity [Feng et al., 2012a] (Figure 1.10d). Zhao *et al.* reported a $MoS_2$ based humidity sensor with a sensitivity of $10^4$ for non-contact sensation [Zhao et al., 2017].

**Table 1.2:** A brief literature survey of humidity sensors.

| S. No | Active Material | Selectivity | Stability, RH% | Type | Time (s) | | Senst. % (RH range, %) | Volt. (V) | Application | Method | Ref. |
|---|---|---|---|---|---|---|---|---|---|---|---|
| | | | | | $R_s$ | $R_r$ | | | | | |
| 1 | $VS_2$ | NA | NA | R | 30-40 | 12-50 | 30 (0-100) | 1 | Touch sensing | 700° C annealing, 18 h | [Feng et al., 2012b] |
| 2 | GO | NA | NA | R | 0.3 | 0.3 | 2 order (30-80) | 1 | Breathing rate | Drop casting and spray coating | [Borini et al., 2013] |
| 3 | GO/PDDA | NA | 60 days, 85% | C | <1s | <1s | 265,640 (11-97) | NG | Breathing rate | Layer-by-layer self-assembly | [Zhang et al., 2014] |
| 4 | Supramolecular nanofibre film | NA | NA | R | 2.2 | 1.05 | 45000 (5-85) | 0.8 | Breathing rate | Solution processable | [Mogera et al., 2014] |
| 5 | Supramolecular nanofibre | NA | NA | R | 8 ms | 24 ms | 400 (5-85) | 0.8 | Breathing rate | Solution processable | [Mogera et al., 2014] |
| 6 | ZnO/GO | NA | 30 days, 85% | C | NG | NG | 2875000 (0-97) | NG | Breathing rate | Layer by layer self assembly | [Wang et al., 2016] |
| 7 | GO/RGO/PDMS | NA | NA | C | NG | NG | 2 order (20-90) | NG | Breathing rate, touch | Layer by layer/CVD | [Ho et al., 2016] |

| | | | | | | | | | | | |
|---|---|---|---|---|---|---|---|---|---|---|---|
| | | | | | | | | | sensing | grown graphene | |
| 8 | GO | NA | 30 days, 95% | R | 1.8 | 11.5 | 3 order (15-95) | 1 | Breathing rate, touch sensing | Femtosecond laser direct writing | [An et al., 2017b] |
| 9 | Si NCs | NA | NA | R | 40 ms | 40 ms | 5 order (8-83) | 5 | Breathing rate, touch sensing | Spin coating | [Kano et al., 2017] |
| 10 | $MoS_2$ | NA | 31 days, 35% | R | 10 | 60 | 4 order (0-35 ) | 30 | Touch sensing | CVD | [Zhao et al., 2017] |
| 11 | CNT/PVA | NA | NA | R | 40 | NG | 220 times | NG | No real application shown | Wet-spinning process | [Zhou et al., 2017a] |
| 12 | PIM | NA | 4 day, 82 % | R | 0.4 | 2.6 | 70 times (11- 82) | 3.3 | Skin moisture sensor | Evap. of polymer gel electrolyte | [Li et al., 2017b] |
| 13 | $WS_2$ | NA | NA | R | 5 | 6 | 2357 (10-90) | 5 | Breathing rate, touch sensing | Sulphurization of sputtered W | [Guo et al., 2017] |
| 14 | RGO/ PU | NA | NA | R | 3.5 | 7 | 9 (10-70) | NG | Touch Sensing | Spin coating/ solution processing | [Trung et al., 2017] |
| 15 | GYD | Yes | 180 days, 86% | R | 7 ms | NG | 18000 (11-95) | 0.5 | Breathing rate | Drop casting | [Yan et al., 2018] |
| 16 | PSS@SNs | $H_2O/NH_3$ | 20 days,95% | R | 2 | 65 | 4 order (33-95) | 1 | Breathing rate | Drop casting | [Zhao et al., 2018a] |
| 17 | poly-MMA-MAPTAC | NA | 60 days, 90% | R | 35 | 310 | 0.0369 log Z/RH% | 1 | Breathing rate | Spray coating | [Xie et al., 2018] |
| 18 | $MoS_2$-$Cu_2S$ | NA | NA | R | NG | NG | 0.57/RH% | NG | Breathing rate | Hydrothermal | [Sahatiya et al., 2018] |
| 19 | Wrinkled graphene | NA | NA | R | 12 ms | NG | 1.5%/RH | NG | Breathing rate, touch sensing | CVD | [Zhen et al., 2018] |
| 20 | GO | NA | NA | C | 2.7 | 4.6 | 4 order (11-97) | - | Touch sensing | Inkjet printing | [He et al., 2018b] |
| 21 | Graphene/ polymer | $H_2O$/ VOCs | NA | R | 20 ms | 17 ms | 4 order (0-97) | 1 | Breathing rate, touch sensing | Drop casting | [He et al., 2018a] |
| 22 | Pt -N-doped RGO | NA | NA | R | NG | NG | 4.51 (2-66.4) | NG | Breathing rate | $H_2$ annealing | [Choi et al., 2018] |
| 23 | Au - polysquaraine | NA | 30 days, 95% | R | 1 | 4 | 5 order (11-95) | 1 | Breathing rate | Drop casting | [Zhou et al., 2018a] |
| 24 | Latex rubber | NA | NA | C | NG | NG | 0.6 pF/RH% | - | Touch sensing | Dicing saw | [Sim et al., 2018] |
| 25 | Au aerogel | NA | NA | R | NG | NG | 2 order (30-80) | NG | Breathing rate | Freeze drying | [Ali et al., 2018] |
| 26 | CNT-PS-*b*-P4VP | NA | 40 mins cont. 95% | R | 0.3 | 3.2 | 800 (10-95) | 2 | NIL | Solution processing, Drop casting | [Shevate et al., 2018] |
| 27 | 2D-$WS_2$ | H2O/VOCs | 3 days,85% | R | 140 | 30 | 3 order (8-85) | 5 | NIL | Drop casting | [Leonardi et al., 2018] |
| 28 | Pencil trace | NA | 30 days, 95% | R | 1 | 12 | 4 order (11-95) | NG | NIL | Pencil drawing | [Zhang et al., 2018f] |
| 29 | $WS_2$/$SnO_2$ | NA | 30 days, 97% | C | 100 | 100 | 5 order (11-97) | - | Breathing rate | LbL self assembly | [Zhang et al., 2018a] |
| 30 | rGO | NA | 1 year | -- | 1.9 | 3.5 | 45 times (6.1-100) | 1 | NIL | Laser direct writing | [Cai et al., 2018] |
| 31 | Silica NPs | NA | NA | R | 5 | 40 | 3 order (11-95) | 1 | NIL | Drop casting | [Zhao et al., 2018b] |
| 32 | Pt -$MoS_2$ | NA | 30 days,65% | R | 92 | 154 | 4000 times ( 25 to 85) | 3.5 | NIL | Drop casting | [Burman et al., 2018] |
| 33 | rGO/$MoS_2$ | NA | NA | R | 17 | 474 | 50 (10-90) | 1 | NIL | e-beam evaporator | [Park et al., 2017a] |

| | | | | | | | | | | | |
|---|---|---|---|---|---|---|---|---|---|---|---|
| 34 | $VO_2$/CNT | $H_2O$/ $O_2$/ $NH_3$ | NA | R | 7 | 60 | 7.1 (50) | 0.1 | NIL | hydrothermal | [Evans et al., 2018] |
| 35 | Carbon nanocoil | NA | 180 days,95% | | 1.9 | 1.5 | 12.2 (4-95) | 0.1 | Breathing rate, touch sensing | CVD | [Wu et al., 2019a] |
| 36 | Ionogel | NA | 30 days,90 % | R | 3 | 10 | 2 order (11-97) | 0.5 | Breathing rate | Inothermal assembly | [Xiao et al., 2019] |
| 37 | PEG/Gold | NA | NA | R | 1.2 | 3 | 4 order (1.8-95) | 5 | Breathing rate | Inkjet printing | [Su et al., 2019] |
| 38 | Flower like $TiO_2$ | NA | NA | R | NG | NG | 485.71 | 7 | Breathing rate | Roll to roll electrode printing | [Jeong et al., 2019] |
| 39 | PMDS poly-electrolyte | NA | 60 days,95% | R | 0.29 | 0.47 | 2 order (11-95) | 1 | Breathing rate, Touch sensing | UV exposure after drop casting | [Dai et al., 2019b] |
| 40 | Quantum dots-chitosan | $H_2O$/ $NH_3$ | 25 days,95% | QCM | 36 | 3 | 39.2 Hz/% (11-95) | - | NIL | Drop casting | [Qi et al., 2019] |
| 41 | Chitosan/ZnO/SWCNT | VOCs | 5 days,75% | R | 200 | NG | 90 (11-97) | NG | NIL | Drop casting | [Dai et al., 2019a] |
| 42 | Organogel (PAM) | NA | 30 days | R | 0.27 | 0.31 | 978 (4-90) | 3 | Breathing rate | Solution processing | [Wu et al., 2019b] |
| 43 | SPEEK/MNS | NA | 30 days,98% | R | 9 | 130 | 5 order (11-95) | 1 | NIL | Dip coating | [Zhuang et al., 2017] |
| 44 | **F-TEDA Crystals** | **yes** | **8 h cont. 95% +20 days,95%** | **R** | **0.04** | **0.40** | **6 order (10-95%)** | **0.8** | **Breathing rate, Touch sensing** | **Drop casting** | [Bahuguna et al., 2020] |

R: Resistive, C: Capacitive; NA: Not Available; NG: Not Given

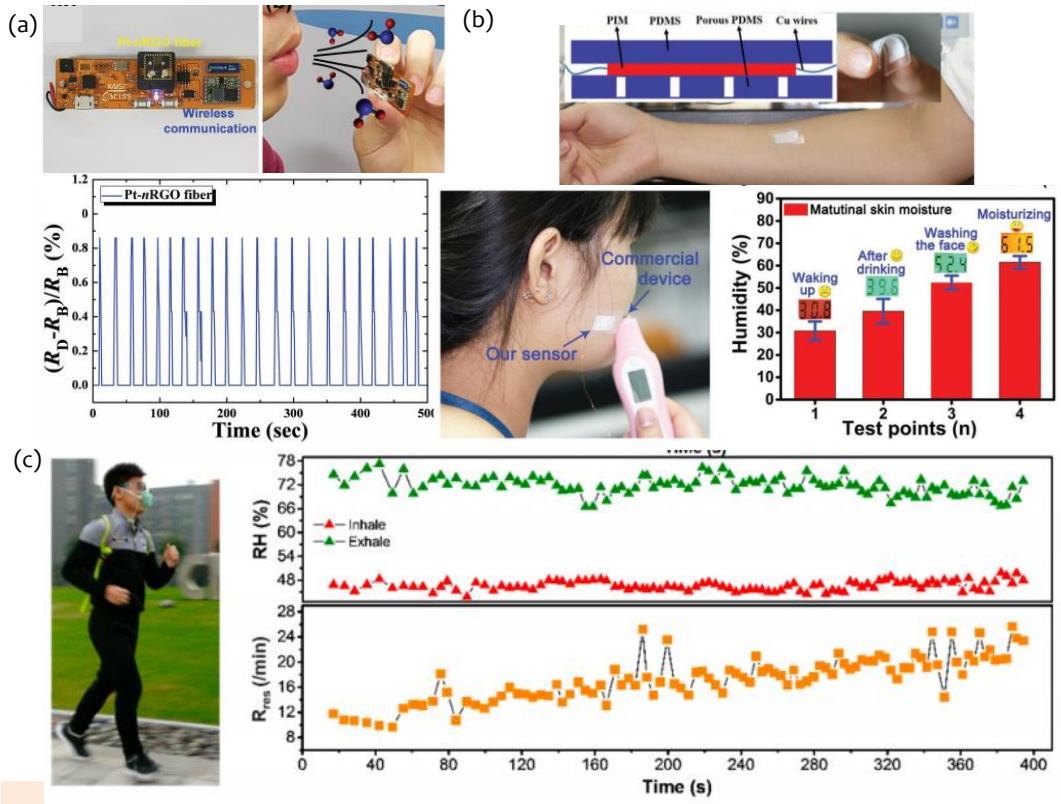


**Figure 1.11:** Application of new generation humidity sensors for (a) breath monitoring (b) skin-moisture sensing and (c) physiological monitoring. Figures in a-c are adapted from [Choi et al., 2018], [Li et al., 2017b] and [He et al., 2018a] respectively.

Recently, the application of humidity sensors for human physiological and psychological monitoring has been tested. Nitrogen-doped graphene fiber based humidity sensor with very high sensitivity is explored for exhaled breath analysis [Choi et al., 2018] (Figure 1.11a). In an another example, humidity sensor based on PIM was explored for skin moisture sensor (Figure

1.11c) [Li et al., 2017b]. He *et al.* recently explored human physiological monitoring via humidity sensor (Figure 1.11b) [He et al., 2018a]. Guo *et al.*, fabricated large area $WS_2$ film on PDMS as electronic skin for moisture sensing with high sensitivity and fast response time [Guo et al., 2017]. A brief literature review of humidity sensors reported in the literature is presented in Table 1.2. However, in some of the reported humidity sensors, some key parameters such as response/recovery, specificity, and stability are compromised at the cost of achieving high values of sensitivity. For example, the humidity sensor based on graphene-polymer composite shows an interference signal for volatile organic compounds despite their high sensitivity [He et al., 2018a]. Bi *et al.* demonstrated a graphene oxide-based sensor with excellent sensitivity with sluggish humidity response of ~10.5 s and recovers slowly in 41 s [Bi et al., 2013].

### 1.7.4 Fluorinated α-$Fe_2O_3$ Nanostructures and its Magnetic Properties

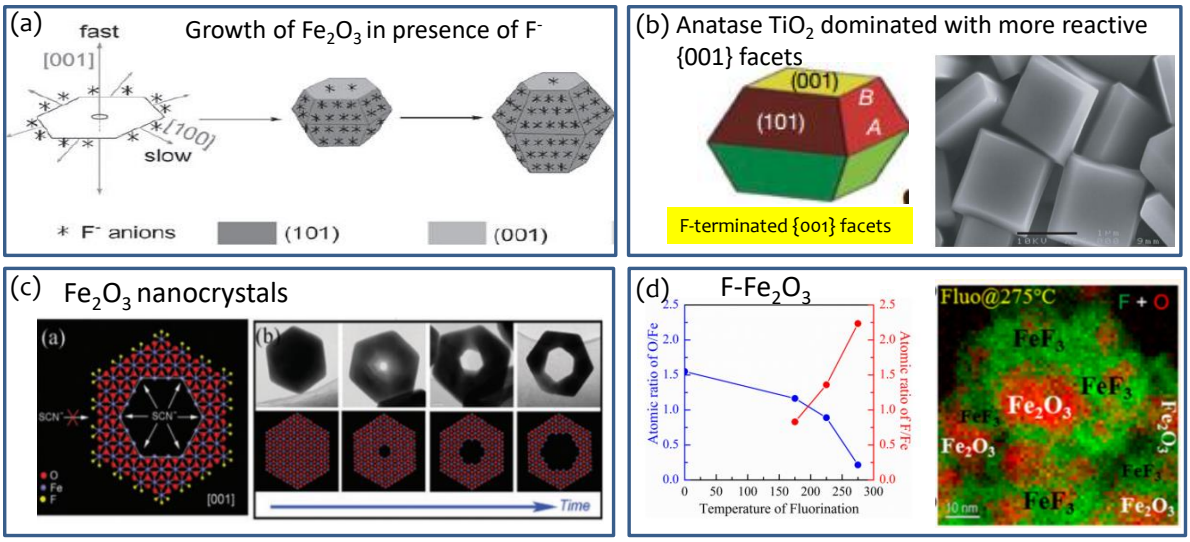


**Figure 1.12:** Synthesis methods for fluorination of metal oxides nanostructures using (a) HF, (b) $TiF_4$, (c) NaF, and (d) fluorine gas as fluorine sources. Figures in a-d are adapted from [Lv et al., 2010], [Yang et al., 2008], [Lv et al., 2011] and [Zhou et al., 2015a] respectively.

Fluorination of metal oxides nanomaterials can be performed post synthetically or during synthesis. In general, the post-synthetic treatment of metal oxides nanomaterials with fluorinating precursors can cause fluorine insertion without any structural change. However, in-situ synthesis can give rise to an altogether different crystal structure [Yu et al., 2010]. Fluorination of metal oxides has been explored in the literature, as shown in Figure 1.12. Among solution-based fluorinating agents, nucleophilic fluorinating sources of HF and $NH_4F$ are generally used; however, these act preferentially as growth directing agents. For example, Lv *et al.* [Lv et al., 2010, 2011] synthesized $Fe_2O_3$ dodecahedral using HF and $Fe_2O_3$ nanocrystal oriented along [001] using NaF as a fluorinating precursor (Figure 1.12a,c). Similarly, Yang *et al.* synthesized 110 faceted $TiO_2$ nanostructures using $TiF_4$ as fluorinating as well as metal source precursor [Yang et al., 2008] (Figure 1.12b). It is observed in the literature that the fluorine is incorporated into the metal oxide lattice when direct fluorination using highly dangerous sources like fluorine gas, $XeF_2$, $ClF_3$, etc. are used. For example, Zhou *et al.* fluorinated $Fe_2O_3$ using fluorine gas and observed a decrease in oxygen content with increasing fluorine giving an indication of substitution doping of $Fe_2O_3$ (Figure 1.12d) [Zhou et al., 2015a].

Nanostructures of Fe and its oxides (hematite, magnetite, and maghemite) have attracted significant attention due to their emerging optical, magnetic, and electronic properties in various practical applications [Mohapatra et al., 2011]. Hematite (α-$Fe_2O_3$), being the most thermodynamically stable, non-toxic, and abundant phase of iron-oxide, is used for photoelectrochemical water splitting [Sivula et al., 2011], photocatalysis [Zhuang et al., 2008], gas sensing [Chen et al., 2005a], photoassisted electrolysis [Quinn et al., 1976] due to its direct

bandgap of 1.95-2.35 eV in the visible range [Al-Kuhaili et al., 2012], and corrosion-resistant nature [Wen et al., 2005]. Fluoride ions are known to influence the α-$Fe_2O_3$ formation by restricting the growth along [100] direction due to adsorption on (100) plane without any fluorination. For fluorination of α-$Fe_2O_3$, various other synthetic methods have been developed that requires the use of either a $FeF_3$ as starting material or a highly reactive $F_2$ or $XeF_2$ gas as a precursor [Brink et al., 2000; Zhou et al., 2015a]. These methods result in the coordination of $F^-$ anions with $Fe^{3+}$ to replace some of the $O^{2-}$ due to their comparable sizes. Fluorination of α-$Fe_2O_3$ either in the form of oxyfluorides or $F^-$ doping has been reported to possess interesting properties that greatly influence the performance of energy storage devices [Brink et al., 2000; Karthikeyan et al., 2014; Zhou et al., 2015a]. Fluorinated α-$Fe_2O_3$ may also find futuristic application in biomedical [Fisicaro et al., 2016], photocatalytic conversions [Kim et al., 2007], nanoelectronics [Ho et al., 2015], superhydrophobicity [Jayaramulu et al., 2016], and other electrochemical-based applications which is yet to be explored.

α-$Fe_2O_3$ is found to be antiferromagnetic in nature (Neel's temperature $T_N \approx 950$ K) that turns weakly ferromagnetic above a certain Morin temperature, $T_M \approx 263$ [Bhowmik et al., 2010]. This weak ferromagnetic behavior of α- $Fe_2O_3$ accompanied with high surface area have been utilized in various applications such as removal of dye from contaminated water [Ranjithkumar et al., 2014], detection of uric acid [Suresh et al., 2014], as nanofluids for heat transfer systems water,[Rufus et al., 2016] lithium storage in lithium-ion batteries [Wang et al., 2011], magnetic data storage and biomedical research. For example, Shan *et al.* [Shan et al., 2014] synthesized high surface area hematite coated maghemite nanoparticles for trace antimony (III) removal and Narayanan *et al.*[Narayanan et al., 2016] used ferromagnetic α-$Fe_2O_3$ for application in drug delivery, cell imaging and cancer theragnosis. The magnetic properties of α-$Fe_2O_3$ are greatly affected by changes in shape, morphology, size distribution and orientation [Jagadeesan et al., 2008; Liu et al., 2013; Wang et al., 2015a]. Spherical α-$Fe_2O_3$ nanoparticles were found to exhibit higher coercivity as compared to rhombohedral-shaped particles [Liu et al., 2013]. The Morin transition temperature is also lowered as the particles become smaller in size. Morin transition for short nanotubes was observed at lower temperatures while no transition was observed for long nanotubes above a critical size indicating size dependence [Wang et al., 2015a]. In an another study by Jagdeeshan *et al.*, hollow α-$Fe_2O_3$ spheres were found to exhibit superparamagnetic behavior [Jagadeesan et al., 2008]. Magnetic anisotropy effects are observed to be dominant in the case of one-dimensional α-$Fe_2O_3$ nanostructures such as nanotubes and nanorods [Liu et al., 2006]. The magnetic properties of α-$Fe_2O_3$ are also tuned by surface modification or by doping with metals and metal oxides[Wu et al., 2006b]. Surface coating of α-$Fe_2O_3$ nanowires with ZnO has been demonstrated to result in high saturation magnetization due to uncompensated surface spins of ZnO shell [Sarkar et al., 2012]. α-$Fe_2O_3$ and $CoFe_2O_4$ nanocomposites were found to exhibit an increase in coercivity with a decrease in the grain size of the composite [Lv et al., 2015]. The effect of different nanostructure on the magnetic property of α-$Fe_2O_3$ is tabulated in Table 1.3.

**Table 1.3** Tabulation of α-$Fe_2O_3$ magnetic parameters reported in the literature.

| S. No. | Shape of $Fe_2O_3$ nanostructures | Morin transition $T_M$ (K) | Coercivity Hc (Oe) | Saturation Magnetization Ms (emu/g) | References |
|---|---|---|---|---|---|
| 1 | $Fe_2O_3$ Nanoring | 210 | NG | 0.303 | [Wang et al., 2015a] |
| 2 | $Fe_2O_3$ Nanowire | 125 | 150 | NG | [Kim et al., 2006] |
| 3 | $Fe_2O_3$ Nanorods (60-90nm) | 255 | NG | NG | [Wu et al., 2006a] |
| 4 | $Fe_2O_3$ Nanorods (5-16nm) | 235 | NG | NG | [Wu et al., 2006a] |
| 5 | $Fe_2O_3$ Hollow | 200 | NG | NG | [Jagadeesan |

| | | | | | |
|---|---|---|---|---|---|
| | Sphere | | | | et al., 2008] |
| **6** | $Fe_2O_3$ Hollow Cup | 250 | 2587 | NG | [Jagadeesan et al., 2008] |
| **7** | $Fe_2O_3$ Micro Pine | 216 | 1510 | NG | [Cao et al., 2005] |
| **8** | $Fe_2O_3$ Nanorod | 166 | 280 | NG | [Liu et al., 2006] |
| **9** | $Fe_2O_3$ Ellipsoid | 251.4 | NG | NG | [Jayanthi et al., 2015] |
| **10** | $Fe_2O_3$ Spindle | 245.4 | NG | NG | [Jayanthi et al., 2015] |
| **11** | $Fe_2O_3$ Fattened | 231.5 | NG | NG | [Jayanthi et al., 2015] |
| **12** | $Fe_2O_3$ Rhombohedral | 220.8 | NG | NG | [Jayanthi et al., 2015] |
| **13** | $Fe_2O_3$ Nanoring | 211 | NG | NG | [Jayanthi et al., 2015] |
| **14** | $Fe_2O_3$ Nanotube | <10 | NG | NG | [Jayanthi et al., 2015] |

NG: Not Given

Different Fe precursors have been used to obtain α-$Fe_2O_3$ nanostructures with different morphologies and magnetic properties [Sayed et al., 2015]. $K_4[Fe(CN)_6]$ is one of the widely used precursors for low-temperature hydrothermal synthesis of dendritic α-$Fe_2O_3$ nanostructures [Bharathi et al., 2010; Cao et al., 2005; Green et al., 2017; Liu et al., 2015b]. There have been several efforts towards understanding the influence of surfactants and additives on the morphology of these dendritic α-$Fe_2O_3$ nanostructures [Majumder et al., 2016]. The magnetic property of these modified nanostructures gets affected even with slight variation in their morphology. For example, Wang *et al.* synthesized the dendritic structures of α-$Fe_2O_3$ and obtained a large coercive field of 1510 Oe with Morin transition at 216 K [Cao et al., 2005]. Interestingly, the coercivity of dendritic α-$Fe_2O_3$ nanostructures was found to increase with a corresponding decrease in saturation magnetization upon conversion to snowflake-type structure [Bharathi et al., 2010]. Like surfactants, different sources of fluoride anions such as $NH_4F$, HF, NaF, and LiF are used in literature to assist the growth process as these adsorb on metal oxide surfaces and act as shape directing agents [Lv et al., 2011; Wang et al., 2015b]. For example, Sun and coworkers synthesized dodecahedral and octahedral α-$Fe_2O_3$ with the aid of fluoride anions with different magnetic behavior [Lv et al., 2010].

### 1.7.5 Fluorinated Tin Oxide for VOC sensors

There are numerous efforts in the literature by doping, functionalization, nanostructuring, faceted growth, heterostructuring, etc. for an efficient VOC sensor. A brief literature survey of VOC sensors based on different inorganic materials is shown in Table 1.4.

**Table 1.4**: Literature summary of VOC sensor using different types of nanomaterials.

| Reference | Material | Synthesis method | Conc (ppm) | LOD (ppm) | Temp (°C) | Analyte |
|---|---|---|---|---|---|---|
| [Chen et al., 2018] | $LaMnO_3/SnO_2$ nanofibers | electrospinning | 100 | NA | 260 | Ethanol |
| [Li et al., 2018] | $WO_3/SnO_2$ nanofibers | Coaxial electrospinning | 10 | NA | 280 | Ethanol |

| | | | | | | |
|---|---|---|---|---|---|---|
| [Choi et al., 2017] | $SnO_2/Fe_2O_3$ nanowires | Hydrothermal and spin coating | 5 | NA | 300 | Ethanol |
| [Wang et al., 2017c] | $SnO_2$ nanocubes | Hydrothermal | 100 | 1 | 200 | Ethanol |
| [Wei et al., 2018] | $SnO_2$ microspheres | Ion exchange method | 200 | NA | 260 | Ethanol |
| [Wang et al., 2017b] | $SnO_2/Fe_2O_3$ microspheres | Hydrothermal | 100 | 0.1 | 260 | Ethanol |
| [Wang et al., 2018] | $SnO_2$ nanospheres | Hydrothermal | 100 | 0.5 | 350 | Ethanol |
| [Zhang et al., 2017c] | $SnO_2$ microtubes | Solvothermal | 100 | 0.01 | 92 | Formaldehyde |
| [Yu et al., 2017] | SnO2 cedar-like structures | Hydrothermal | 100 | 1 | 200 | Formaldehyde |
| [Xie et al., 2018] | $Pd/SnO_2$ nanofibers | Electrospinning and carbonization | 100 | 0.5 | 250 | Toluene |
| [Zhang et al., 2017b] | $Pd/SnO_2$ microspheres | Hydrothermal | 20 | 0.1 | 230 | Toluene |
| [Qiao et al., 2017] | $Pd/SnO_2$ cubic nanocages | Self-sacrificial template and precipitation | 20 | 0.1 | 230 | Toluene |
| [Zhang et al., 2018b] | $Sm_2O_3/SnO_2$ nanorods | Hydrothermal | 100 | NA | 260 | Acetylene gas |
| [Li et al., 2017a] | $SnO_2/Fe_2O_3$ nanospheres | Self-sacrificial template | 100 | NA | 260 | Acetone |
| [Li et al., 2017c] | $SnO_2$ hierarchical | Hydrothermal | 100 | 0.05 | 325 | Acetone |
| [Shinde et al., 2018] | $Bi_2O_3$ Nanostructures film | Successive ion exchange | 100 | 10 | 27 | Acetone |
| [Koo et al., 2017] | $PdO\text{-}Co_3O_4$ hollow nanocages | Encapsulated via infiltration | 5 | 0.1 | 350 °C | Acetone |
| [Zhang et al., 2018e] | Hierarchical $Co_3O_4$ Structures | Coprecipitation/ spray pyrolysis | 200 | NA | 190 | Acetone |
| [Zhou et al., 2017b] | $Co_3O_4$ nanosphere | Hydrothermal | 500 | NA | 220 | Acetone |
| [Zhang et al., 2018d] | MWCNTs/ $Co_3O_4$ nanocube | Hydrothermal | 100 | NA | 120 | Acetone |
| [Geng et al., 2018] | α- $Fe_2O_3$ bimodal porous | Hydrothermal | 100 | NA | 300 | Acetone |
| [Zhang et al., 2018c] | $LaFeO_3$/α- $Fe_2O_3$ Porous Nanooctahedrons | Hydrothermal | 100 | NA | 230 | Acetone |
| [Liu et al., 2018b] | $In_2O_3$ Pt nanowires | One-step co-electrospinning method | 1 | .01 | 320 | Acetone |
| [Zhou et al., 2018b] | $NiO/NiCo_2O_4$ Truncated Nanocages with PdO Catalyst | Coprecipitation method | 100 | NA | 210 | Acetone |
| [Osica et al., 2017] | Porphyrin | Chemical method | 100 | 1 | 37 | Acetone |
| [Ma et al., 2017] | $ZnO/ZnFe_2O_4$ MOF | Chemical method | 5 | NA | 250 | Acetone |
| [Song et al., 2017] | $ZnFe_2O_4$ Hollow Octahedral Nanocages | Thermal decomposition | 200 | NA | 120 | Acetone |

There have been many efforts to bring down the operating temperature by surface engineering of the oxide via designing of hybrid nanomaterials [Xu et al., 2020], doping [Xu et al., 2015], faceted or 1-D growth [Chen et al., 2015; Haddad et al., 2018], and hetero-structuring and complementing sersor wih UV illumination [Chen et al., 2015; Sharma et al., 2018; Yang et al., 2019] (Figure 1.13a-d). This way, the chemical and physical properties of the oxide can get modified, accelerating gas diffusion on the surface, thereby shortening the response time and lowering the working temperature. $SnO_2$ hybrids with CNTs [Yan et al., 2019], graphene oxide [Salehi et al., 2014], GaN [Bajpai et al., 2012], ZnO core-shell nanostructure [Kalidoss et al., 2019], and metal dopants Pt [Poloju et al., 2017], Au [Moon et al., 2019][Quan et al., 2020], Pd[Moon et al., 2019], Ni [Tan et al., 2011], and their oxides) have exhibited improvement in the VOC sensing performance in contrast to pristine $SnO_2$ (Figure 1.13 a-d).

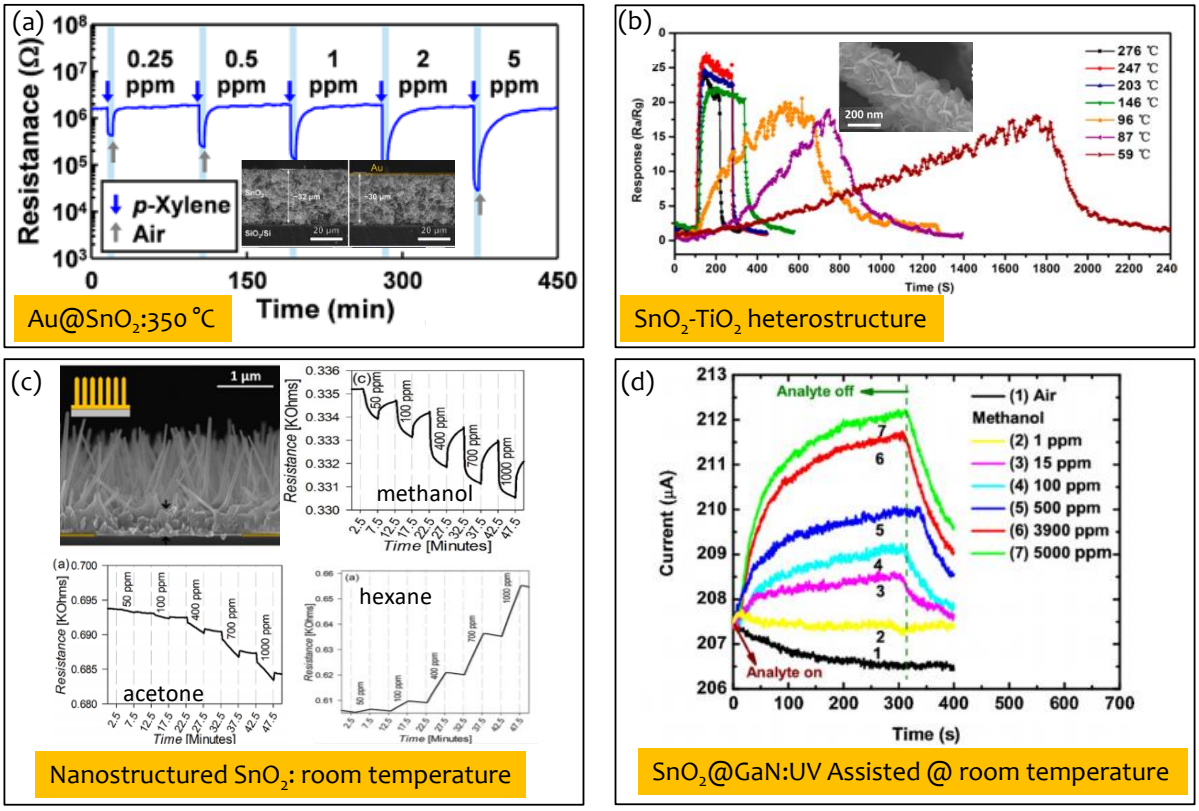


**Figure 1.13:** Brief literature for enhancing the performance of $SnO_2$ based VOC sensor. (a) Au doped $SnO_2$, (b) $SnO_2/TiO_2$ heterojunction (c) $SnO_2$ Nanostructuring and (d) $SnO_2$@GaN. Figures in a-d are adapted from [Moon et al., 2019], [Chen et al., 2015], [Haddad et al., 2018] and [Bajpai et al., 2012] respectively.

Surface fluorination of metal oxide (~ 5-10 nm) can accelerate the reaction process and lower the operating temperature of sensors. Surface fluorination of metal oxides can increase the surface electric conductivity and charge density [Sysoev et al., 2017]. A brief literature survey of fluorinated materials used for VOC sensing applications is presented in Table 1.5. Other than fluorocarbons, there are only two reports on fluorinated-$SnO_2$ for sensing of $NO_2$ and LPG gas [Kemnitz et al., 1998; Wang et al., 2013a].

**Table 1.5:** Literature survey of the fluorinated materials used for sensing applications.

| Material | Fluorinating Precursor | Synthesis method | Conc (ppm) | LOD (ppm) | Temp (°C) | Analyte | Ref. |
|---|---|---|---|---|---|---|---|
| CNT | Ar:$F_2$ and $CF_4$ plasma | microwave (MW) plasma fluorination of CCVD grown CNT | 10 | NA | RT | $NH_3$, $NO_2$ | [Struzzi et al., 2019] |
| Graphene oxide | XtalFluor-E | Chemical fluorination | 0.1 | 0.006 | RT | $NH_3$ | [Kim et al., 2017] |

| | | using | | | | | |
|---|---|---|---|---|---|---|---|
| Fluorinated MOF | $(AlF_5(OH_2))^{2-}$ $(NbOF_5)^{2-}$ | Chemical synthesis | 25 | NA | RT | $SO_2$ | [Tchalala et al., 2019] |
| Fluorinated graphene ink | FG powder dispersed in IPA | Sonication | 20%- 70% (RH) | NA | RT | Humidity | [Hajian et al., 2019] |
| Fluorinated graphene | $SF_6$ | Gas phase fluorination | -- | NA | RT | Photo-detector (UV, visible and NIR) | [Xu et al., 2019] |
| Fluorinated graphene | $SF_6$ | Gas phase fluorination | 2 | NA | RT | $NH_3$, CO | [Zhang et al., 2016a] |
| Fluorinated graphene | Graphite Fluoride, | Hummers method | 2 | NA | 400 | $NH_3$ | [Kang et al., 2018] |
| F-$SnO_2$ | $NH_4F$ | Dip coating | 25 % LEL | NA | 300 | LPG | [Chaisitsak, 2011] |
| $SnO_2$ and fluorine modified graphene | $F_2$ gas | thermal fluorination of $SnO_2$ modified graphene | 50 | NA | 400 | NO | [Kim et al., 2019] |
| F- $SnO_2$ | $NH_4F$ | Hydrothermal | 33 | NA | RT | $NO_2$ | [Wang et al., 2013a] |
| Fluoro-graphene | Fluorinated graphite polymer | Solution Processing | 1 pM | 0.4pM | RT | $NH_3$ | [Tadi et al., 2016] |

## 1.8 Objectives and Scope of the Thesis

Energy production and storage is one of the key research areas as the development of a society conjugate with increasing energy demands. Energy production via different renewable and non-renewable sources require efficient energy storage devices that can store and deliver energy as per the requirement. The survival of human generation with better standards of living along with no/minimal harm to the natural ecosystem is dependent on an unlimited supply of renewable energy, its storage, and state-of-the-art healthcare facilities. These energy and healthcare demands in some way or the other, rely on new generation advanced materials and devices. Therefore, the development of highly efficient synthetic methods, novel materials, and fabrication of unconventional devices are key challenges that are addressed in this thesis. Recently, fluorine chemistry has gained tremendous attention in the area of electrochemical energy devices such as lithium ion batteries, fuel cells and solar cells. With the advent of new fluorinating systems and methods, it is interesting to study the effect of fluorine on the electrochemical characteristics of such energy devices.

The overall objective of this thesis work is focused on synthesis of nanomaterials and characterization of morphological, structural, physical, chemical, optical, magnetic and electrochemical changes in the properties on their fluorination for enabling applications in energy and healthcare.

The scope of each research chapter (3-7) of the thesis work is as follows:

1. Carbon based materials have been extensively explored for energy storage applications however, the low quality of cheap source carbon still supresses its large scale utility. To serve the purpose, electrophilic fluorination of commercially available low cost activated carbon has been performed using F-TEDA as a fluorinating precursor at milder solution processable conditions. Further, the fluorinated carbon material is explored as an electrode material in two-electrode geometry resulting in enhanced supercapacitive performance.

2. We have explored an electrophilic N-F fluorinating agent, Selectfluor (F-TEDA) as a co-electrolyte with conventional organic electrolyte for application in electric double layer supercapacitors. F-TEDA is chosen as an additive to $TBABF_4$ electrolyte due to its moderate solublity in polar solvents however it has good ionic conductivity and structural similarity with the conventional electrolytes The work is focussed on the electrochemical behavior of the electrolyte system in an electric double layer supercapacitor (EDLC) assembly for overall improvement in the capacitive performance.

3. Humidity Sensors have recently gained importance as a wearable health monitoring device. Towards this goal, a highly sensitive sensor with extremely high specificity, stability and spontaneity in real life humidified conditions is developed. In this work, we have explored for the first time organic crystals of electrophilic N-F fluorinating agent, Selectfluor (F-TEDA) as an active sensing material. The material is quite fascinating due to its anisotropic crystalline shape, structural properties and most importantly the selective interaction behavior with water molecules. The humidity sensor is fabricated in the form of a prototype for breath monitoring and touch-less skin moisture sensor as a wearable healthcare device. The sensor is unique due to its exceptional specificity only towards moisture which is reported for the first time in this study.

4. A hydrothermal synthetic strategy is developed for the in-situ preparation of surface fluorinated $\alpha$-$Fe_2O_3$ by using Selectfluor as an electrophilic source for fluorine in the form of $F^+$. The results are compared with other solution based fluorides that plays a passive role instead of acting as a fluorinating agent. We focus on the structure and morphological changes introduced by the fluorine precursors that can potentially influence the magnetic properties.

5. In this chapter, a surface fluorination of $SnO_2$ film by solution-processed method using Selectfluor™ as a fluorinating agent is developed. Even though F-$SnO_2$ is well known as a transparent conductor, its sensing capabilities are relatively unexplored. The simplicity of method adopted for surface fluorination, advantage of low temperature operation and the novel approach adopted for the sensor-reset design for a transparent VOC sensor are important aspects of this work.

## 1.9 Conclusions

The introductory chapter of the thesis presented the basics of nanomaterials and their specific importance in the field of energy and gas sensing devices. Further, the modification of nanomaterials via doping is discussed for the tailoring of properties for the specific application. Fluorine as a dopant for inorganic metal oxides and carbon material is summarized with its application in vast field of interest. In the upcoming chapters, the synthesis and application of fluorinated materials for energy and sensing applications is elaborated.